

# Liquid metal embrittlement in laser lap joining of TWIP and medium-manganese TRIP steel: The role of stress and grain boundaries

M.H. Razmpoosh<sup>a,\*</sup>, E. Biro<sup>a</sup>, D.L. Chen<sup>b</sup>, F. Goodwin<sup>c</sup>, Y. Zhou<sup>a</sup>

<sup>a</sup> Centre for Advanced Materials Joining, Department of Mechanical & Mechatronics Engineering, University of Waterloo, 200 University Avenue West, Waterloo, Ontario N2L 3G1, Canada

<sup>b</sup> Department of Mechanical and Industrial Engineering, Ryerson University, 350 Victoria Street, Toronto, Ontario M5B 2K3, Canada

<sup>c</sup> International Zinc Association, Durham, NC 27713, USA

## ARTICLE INFO

### Keywords:

Fiber laser welding  
Twinning induced plasticity steel  
Transformation induced plasticity steel  
Liquid metal embrittlement (LME)  
Microstructure

## ABSTRACT

High-Manganese austenite-containing steels with superior combination of strength and ductility have shown potential for enhancement of passenger safety and body-in-white (BIW) weight reduction. Even though Zn-coated austenitic steels have improved corrosion resistance, they are highly susceptible to liquid metal embrittlement (LME) during welding. The present work is aimed to address LME susceptibility during restrained laser lap joining of high-Mn twinning induced plasticity (TWIP) and medium-Mn transformation induced plasticity (MMn-TRIP) steels. Electron probe micro-analysis (EPMA) results showed that stress-assisted diffusion of Zn into the austenite grain boundaries and further liquid Zn formation by a peritectic reaction lead to grain boundary decohesion. Electron backscatter diffraction (EBSD) results demonstrated that high angle and special grain boundaries are prone to Zn-penetration within the heat-affected-zone (HAZ). Additionally, LME sensitivity was observed to be highly dependent on the magnitude of applied stress.

## 1. Introduction

In recent years, austenite-containing advanced high strength steels (AHSSs) have received significant commercial and research interest because of their exceptional combination of strength and ductility for automotive applications. Among the best known are the classes of twinning induced plasticity (TWIP) and medium-Mn transformation induced plasticity (MMn-TRIP) steels, in which the austenite phase is stabilized by the addition of high amounts of Mn [1,2]. High volume fraction of austenite provides a high work-hardening rate through mechanical twinning and the deformation-induced martensitic transformation in TWIP and TRIP steels, respectively [3–6]. Zn-based coatings are most commonly used to protect TWIP and MMn-TRIP steels from environmental corrosion; however, the co-presence of a high austenite fraction and Zn-coating has been found to result in severe sensitivity to liquid metal embrittlement (LME) during resistance spot welding [7–9]. This could impede the adoption of these steels into automotive designs.

Based on Gleeble thermomechanical simulation results, Beal et al. [10] reported a drastic reduction in fracture strength and ductility in electrogalvanized (EG) 22Mn-0.6C full austenitic TWIP steel between 700 and 950 °C. Moreover, LME became more severe when Gleeble tests

were carried out with reducing holding times at elevated temperatures before the application of tensile stress. At longer holding times, the formation of Fe-Mn-Zn intermetallic compounds at the steel-Zn interface suppressed embrittlement [10]. In other words, by consumption of liquid Zn through the formation of intermetallic compounds, a lower amount of liquid Zn remaining for embrittlement under stress. It was also suggested that the presence of intermetallic phases could act as a barrier between the steel and liquid Zn [10]. From a practical point of view, during welding, areas of the weld zone are exposed to tensile loading and a temperature range of 700–950 °C for short times. Resistance spot welding (RSW) and laser beam welding (LBW) are considered as the main joining methods for thin sheets in the automotive industries. So far, several researchers showed that Zn-coated TWIP steels are prone to liquid zinc embrittlement during RSW. Ashiri et al. [11] showed that, LME could considerably affect the weldable current range of Fe-15Mn-0.5C-2Al TWIP steel. Higher peak temperatures induced by the high electrical resistivity of TWIP steel (rapid nugget growth) and simultaneous presence of liquid Zn resulted in a severe LME cracking. Moreover, it has been shown that the sensitivity of Zn-LME is highly reliant on Zn-coating type. In this regard, Galvanized (GI)-coated TWIP steel possesses the highest susceptibility, compared to Galvannealed (GA) and EG-coatings [12]. The current range of GI-

\* Corresponding author.

E-mail address: [mhrazmpoosh@uwaterloo.ca](mailto:mhrazmpoosh@uwaterloo.ca) (M.H. Razmpoosh).

**Table 1**  
The chemical composition (wt%) of the experimental TWIP and MMn TRIP steels.

| Steel    | C    | Mn   | Si   | P    | S     | Al   | Fe   |
|----------|------|------|------|------|-------|------|------|
| TWIP     | 0.48 | 14.1 | 0.04 | 0.01 | 0.001 | 1.95 | Bal. |
| MMn-TRIP | 0.15 | 10.4 | 0.17 | 0.01 | 0.010 | 1.49 | Bal  |

coated TWIP steel was found to be reduced by over 77% to prevent LME cracking while still producing acceptable quality weld nuggets [11].

In contrast to several studies on LME susceptibility during RSW of TWIP and TRIP steels [11–14], there is a lack of knowledge on LME sensitivity during LBW of austenitic TWIP and the new class of austenitic-ferritic MMn-TRIP steels. It is suspected that the presence of liquid Zn during laser welding and the stress generated due to clamping could lead to LME crack formation and therefore, affects the structural integrity of the joints and performance of the parts. Hence, the main motivation of the present study is to provide an understanding of LME

during restrained laser welding of TWIP and MMn-TRIP steels and the underlying embrittlement mechanism.

## 2. Material and Experimental Procedure

The chemical compositions of the experimental TWIP and MMn-TRIP steels are given in Table 1. The MMn-TRIP steel sheets (1.45 mm thick) were GI-coated (coating weight of 50 g/m<sup>2</sup> per side) and the TWIP steel sheets (1.2 mm thick) were bare. Laser welding was performed using a fiber laser system (YLS-6000-S2) with a maximum power output of 6 kW, equipped with a Panasonic robotic arm. The fiber core diameter, the spot size, and the beam focal length were 0.3, 0.6, and 200 mm, respectively. During all welding trials, the laser beam remained focused on the surface of the upper sheet. The constraint setup, specimen, and laser welding head configuration are depicted schematically in Fig. 1a. The lap-joining specimen geometry is shown in Fig. 1b. To investigate LME cracks and microstructure, samples parallel to the welding direction were prepared for analysis. Of particular

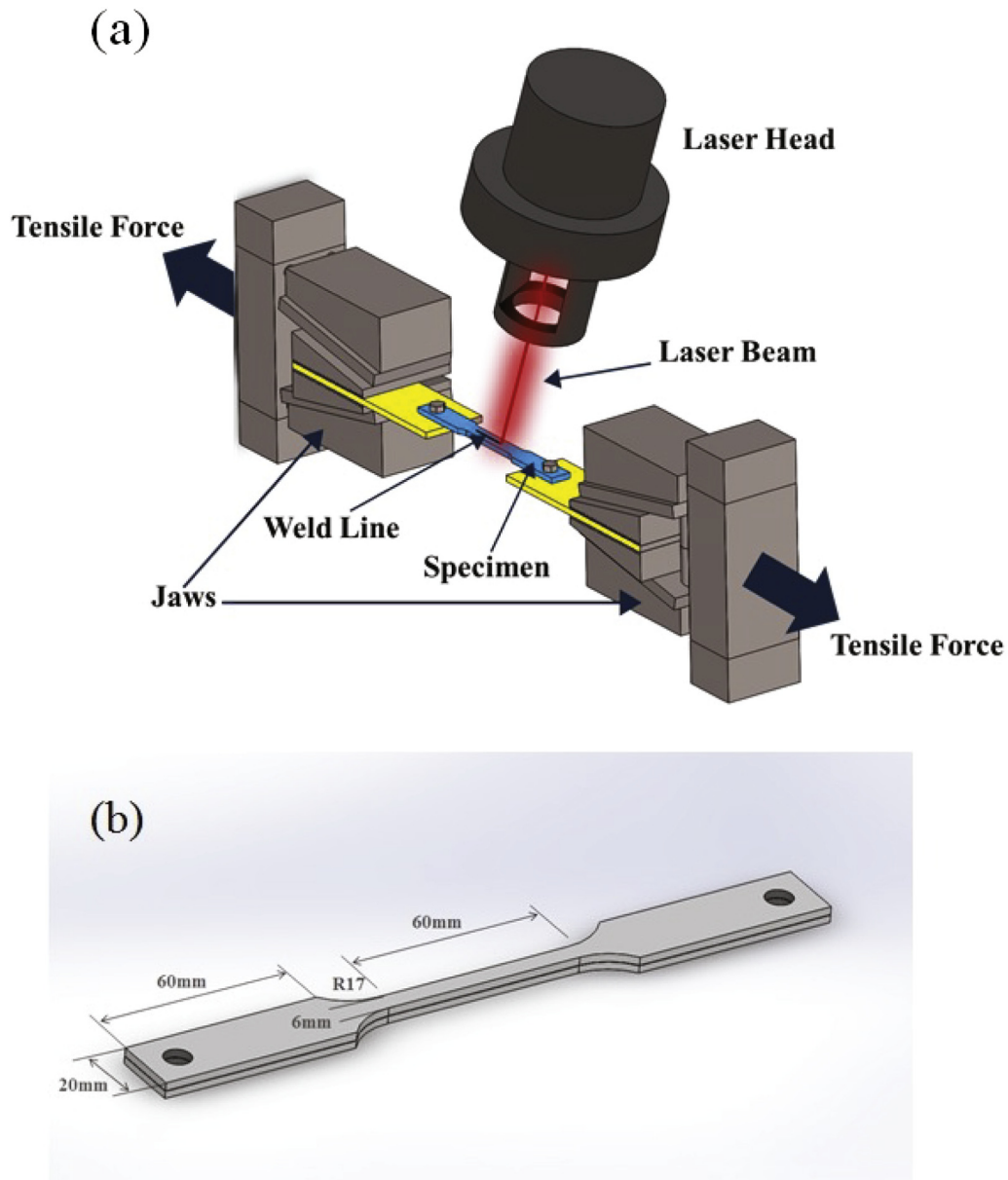


**Fig. 1.** (a) The developed setup to apply external loading during laser lap welding, and (b) schematic illustration of the lap joining specimen geometry and configuration.

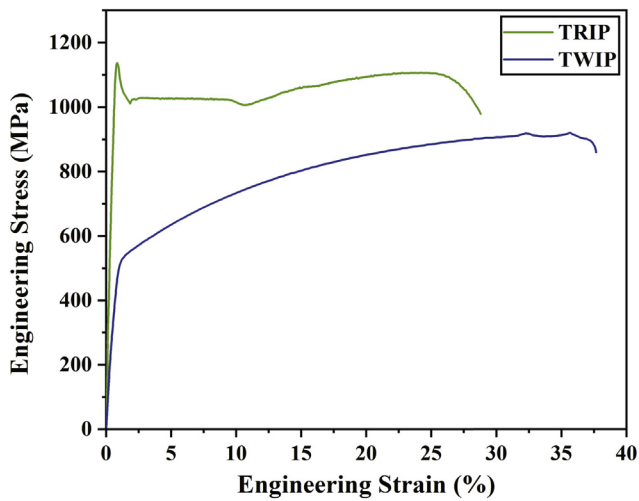


Fig. 2. Engineering stress-strain curves of the experimental TWIP and MMn-TRIP steels.

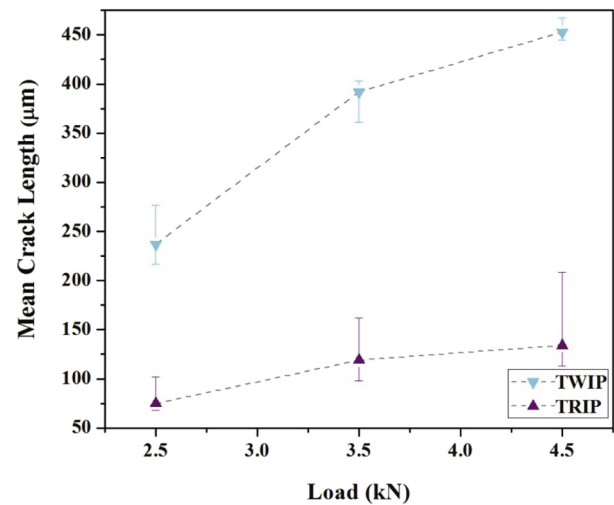


Fig. 4. Mean crack length versus the applied load in the TWIP and MMn-TRIP side of the joint.

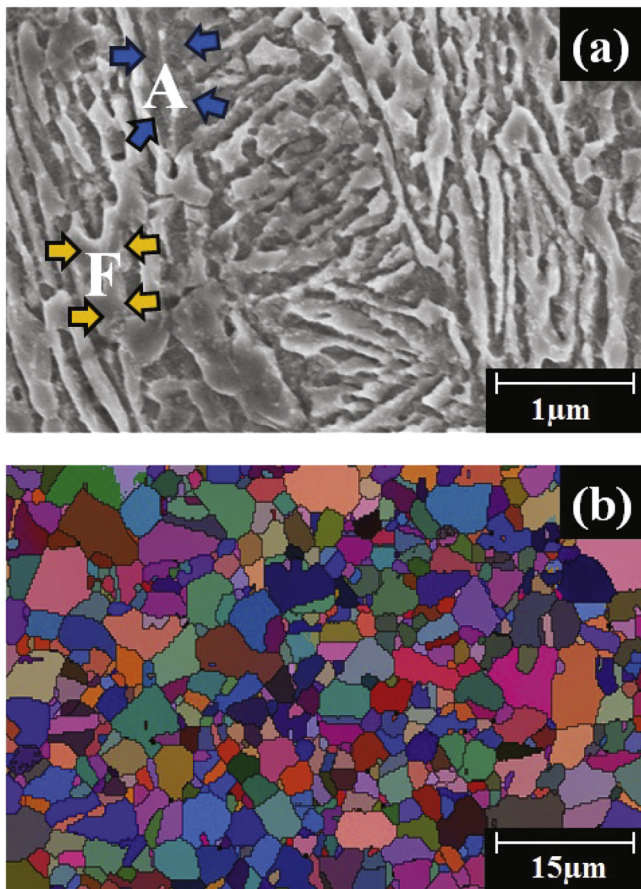


Fig. 3. The initial microstructure of (a) MMn-TRIP, and (b) TWIP steels (A: austenite and F: ferrite).

interest were observations of the heat-affected zone (HAZ). LME cracks were studied by means of scanning electron microscopy (SEM), equipped with energy-dispersive spectroscopy (EDS) and wavelength-dispersive spectroscopy (WDS). Detailed analysis of the microstructure and the grain boundaries was performed by electron backscatter diffraction (EBSD) technique. The EBSD samples were mechanically polished using oxide polishing suspension (OPS) suspension. The EBSD analysis was carried out by JEOL JSM 7000f field-emission gun SEM

equipped with the HKL Technology EBSD system. The acquisition of data was carried out by the Oxford Instruments Aztec software. For EBSD measurements, a step size of  $0.25 \mu\text{m}$ , working distance of about  $15 \text{ mm}$  and an accelerating voltage of  $20 \text{ kV}$  were used. The post-processing of the collected data was performed by HKL Channel 5 software. Low-angle boundaries (LABs) and high-angle boundaries (HABs) were defined as grain boundaries with a misorientation of  $0.7^\circ < \theta < 15^\circ$  and  $\theta > 15^\circ$ , respectively. To determine the LME cracking susceptibility various criteria such as the maximum crack length, overall number of cracks and total length of cracks have been used by the other researchers [15]. In the present study to determine the LME sensitivity, the maximum crack length criterion has been used as longer cracks could propagate much rapidly under the applied tensile stresses. Fig. 2 shows the engineering stress vs. strain curves of the as-received TWIP and MMn-TRIP steels. The results showed yield strength of about  $530$  and  $1100 \text{ MPa}$  for TWIP and MMn-TRIP steel, respectively.

### 3. Results and Discussion

#### 3.1. As-Received Microstructure

The initial microstructures of the as-received TWIP and MMn-TRIP steels are shown in Fig. 3. According to Fig. 3a, the MMn-TRIP steel microstructure consisted of an ultrafine lamellar austenite in a ferrite matrix. The mean austenite lamella width was approximately  $120 \text{ nm}$ . By means of image processing, the austenite volume fraction in the initial structure was determined to be about  $50\%$ . The lamellar austenite structure agrees with previous research on MMn-TRIP steel [16]. In contrast, the EBSD analysis confirmed a full austenitic microstructure of TWIP steel with a mean grain size of about  $3 \mu\text{m}$  (Fig. 3b).

#### 3.2. Effect of the External Tensile Stress on LME Susceptibility

As described by several researchers [10,17,18], the simultaneous presence of sufficiently high tensile stresses and a liquid film in a sensitive polycrystalline material leads to grain boundary decohesion. To investigate the role of a tensile load on the LME cracking, LBW trials have been performed under different external loading conditions. The average maximum length of LME-cracks in TWIP and MMn-TRIP steel versus the applied external load is depicted in Fig. 4. The results show that the LME crack length increases with increasing applied load, where TWIP steel shows longer cracks compared to TRIP steel (i.e. higher LME susceptibility in the TWIP steel). According to Fig. 2, the yield strength of TWIP steel is much lower than that of the TRIP steel. Hence, in



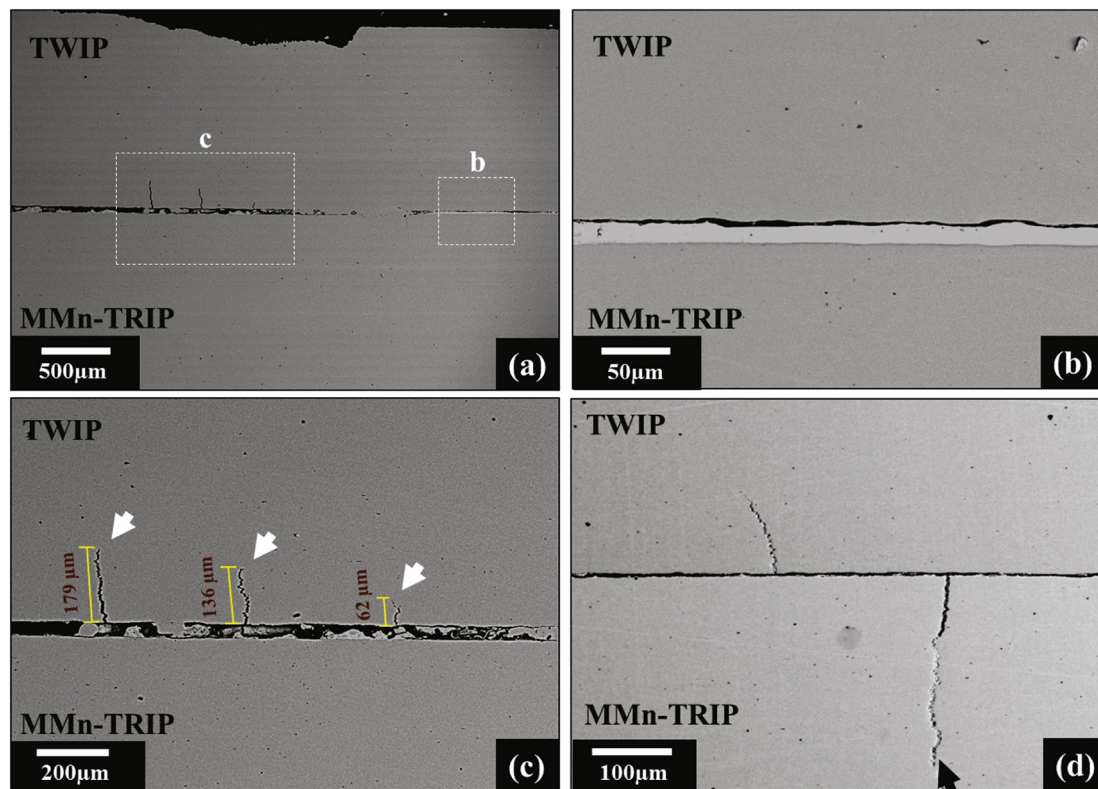


Fig. 5. SEM micrographs showing (a) overview of LME cracks formed within the HAZ, (b) Zn-coating between two sheets, (c) LME cracks in TWIP side of the joint, and (d) representative LME crack in MMn-TRIP side of the joint (black arrow).

addition to higher austenite volume fraction in the TWIP steel, higher LME susceptibility in the TWIP steel can be attributed to the lower yield strength of the material. The observed correlation between the applied stress and crack length is in accordance with the proposed mechanism of LME in the present study.

### 3.3. LME Crack Characterization

Fig. 5 illustrates the occurrence of multiple LME cracks with different lengths after restrained LBW. As described before, sectioning and grinding were carried out parallel to the welding direction to analyze LME crack within the HAZ. The results from various welding conditions indicated that all LME cracks initiated from the TWIP-TRIP interface (Fig. 5a and b), where Zn-coating from the TRIP side of the joint penetrated into the both sides of the joint. Even though TWIP steel is not coated, the liquid zinc from the TRIP side of the joint penetrated along the grain boundaries within the HAZ from the joint interface and created several LME cracks under the applied external stress. The length of the LME cracks are of the order of 100  $\mu\text{m}$  (Fig. 5c), which is much longer than the acceptable crack length of 10  $\mu\text{m}$  [19]. In addition, as Fig. 5d shows LME cracking has also occurred in the TRIP side of the joint; however, it has been observed that the total number of LME cracks and the maximum crack length are lower than on the TWIP side of the joint.

Fig. 6a shows EDS Fe and Zn element mapping of a representative LME crack region in the TWIP side of the joint. As seen, a considerable amount of Zn is present inside the crack where it penetrated very deep along the crack. The temperature within the HAZ during fiber laser welding of AHSSs exceeds 700  $^{\circ}\text{C}$ , where it falls between Zn melting and boiling points of 419 and 907  $^{\circ}\text{C}$ , respectively [20]. Accordingly, the GI-coating transforms into liquid phase above HAZ and penetrates along the grain boundaries during LBW. Fig. 6b and c demonstrate the detailed electron probe micro-analysis (EPMA) Zn distribution maps at the middle and the tip of the LME crack. From Fig. 6b and c, it may be seen

that the Zn content at the tip of the crack is less than at the middle length of the crack. Ashiri et al. [12] and Kang et al. [21] also observed a similar change in Zn concentration along the LME crack length. As described earlier [12], a lower Zn content at the crack tip is an indication that grain boundary based diffusion is mainly responsible for the Zn-penetration. The line profiles in Fig. 6d reveal the Zn content inside the LME crack match the composition of the  $\Gamma\text{-}(\text{Fe,Mn})_3\text{Zn}_{10}$  phase (72–76.5 wt% Zn) [21]. Moreover, the elemental analysis confirmed the presence of 4–5 wt% of Mn and  $\sim 1$  wt% of Al inside the crack. The existence of Mn and Al shows that liquid-Zn phases dissolved Mn and Al from the austenite matrix. In agreement with Fe-Mn-Zn ternary phase diagrams [22], the previous studies [21,23] also indicated the presence of  $\Gamma\text{-}(\text{Fe,Mn})_3\text{Zn}_{10}$  phase in the central regions of LME-cracks. According to Kang et al. [21], during high temperature processing of austenitic TWIP steel one may expect multiple formation and propagation stages. First, in the heating cycle of LBW  $\eta$ -phase (main phase of GI-coating) transforms into the liquid phase. Second, Zn penetrates into the austenite grain boundaries through the stress-assisted diffusion mechanism. The presence of a much lower Zn content at the tip of the crack is also an evidence of a diffusion-based mechanism of Zn penetration. However, the very large penetration depth of Zn (hundreds of micrometers) cannot be justified by only Zn-diffusivity along the austenite grain boundaries. In other words, the observed depth of Zn penetration is orders of magnitude higher than the predicted solid-state diffusion distance of Zn atoms in the short time period of laser welding. Therefore, the considerable depth of Zn penetration is attributed to the stress-assisted diffusion mechanism [21,24]. As a result of Zn accumulation in the grain boundary, Zn content exceeds the maximum solubility limit in austenite [21]. Over the maximum solubility limit, liquid-Zn starts to form along the austenite grain boundaries. Afterwards, as a consequence of liquid-Zn film presence along grain boundaries, the metallic bond weakening takes place due to the adsorption-induced decohesion theory [18], and subsequently, the initial LME crack opens up. It is most likely that by the crack opening, more liquid-Zn from the

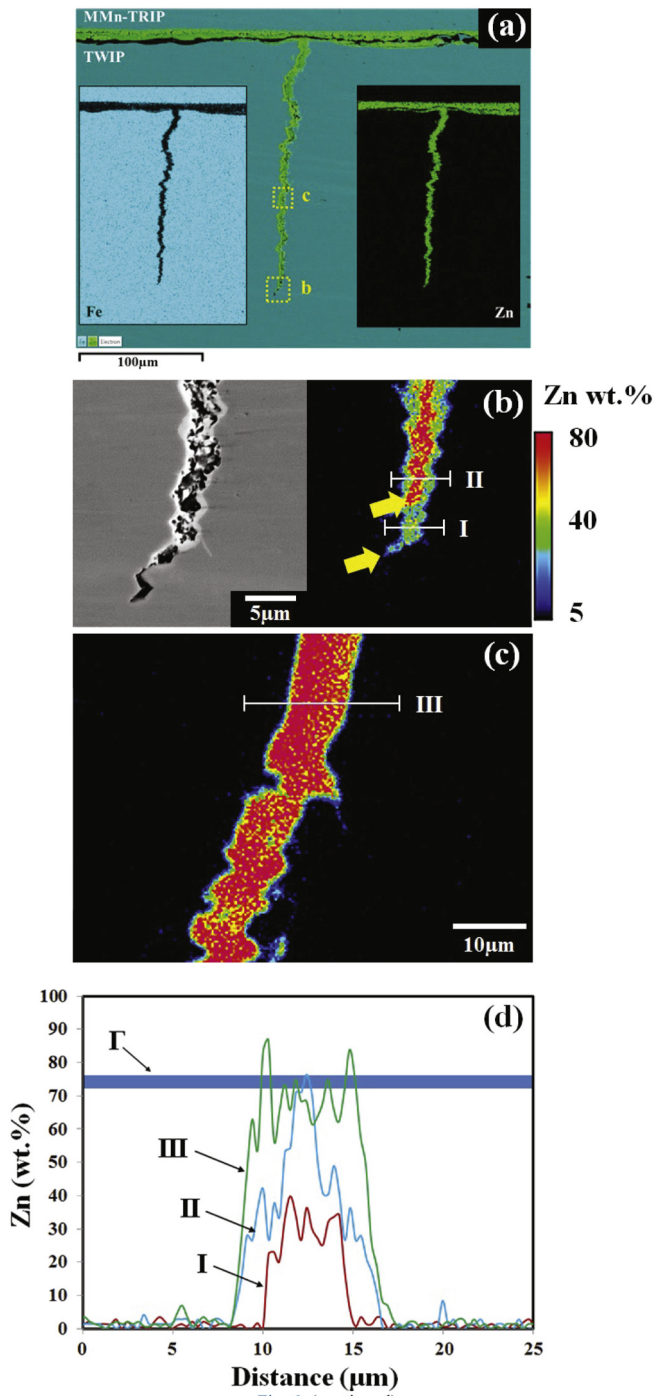


Fig. 6. (a) EDS elemental map of the LME-crack showing the Zn-penetration, EPMA analysis at (b) tip, (c) middle part of the LME crack, and (d) Zn concentration profile in various regions of the LME crack and  $\Gamma$ -phase Zn-content range.

melted GI-coating flow into the crack through a well-established capillarity effect. More fresh liquid-Zn inside the crack promotes further Zn-penetration and eventually under the applied tensile stresses LME-crack could propagate even more rapidly. During the cooling phase of the weld cycle and after crack propagation ended, the liquid phase inside the crack and the austenite matrix in the vicinity of crack (composed of Fe and Mn in addition to Zn due to matrix solid-state diffusion) tend to transform into  $\Gamma$ -(Fe,Mn)<sub>3</sub>Zn<sub>10</sub> phase through the following peritectic reaction:

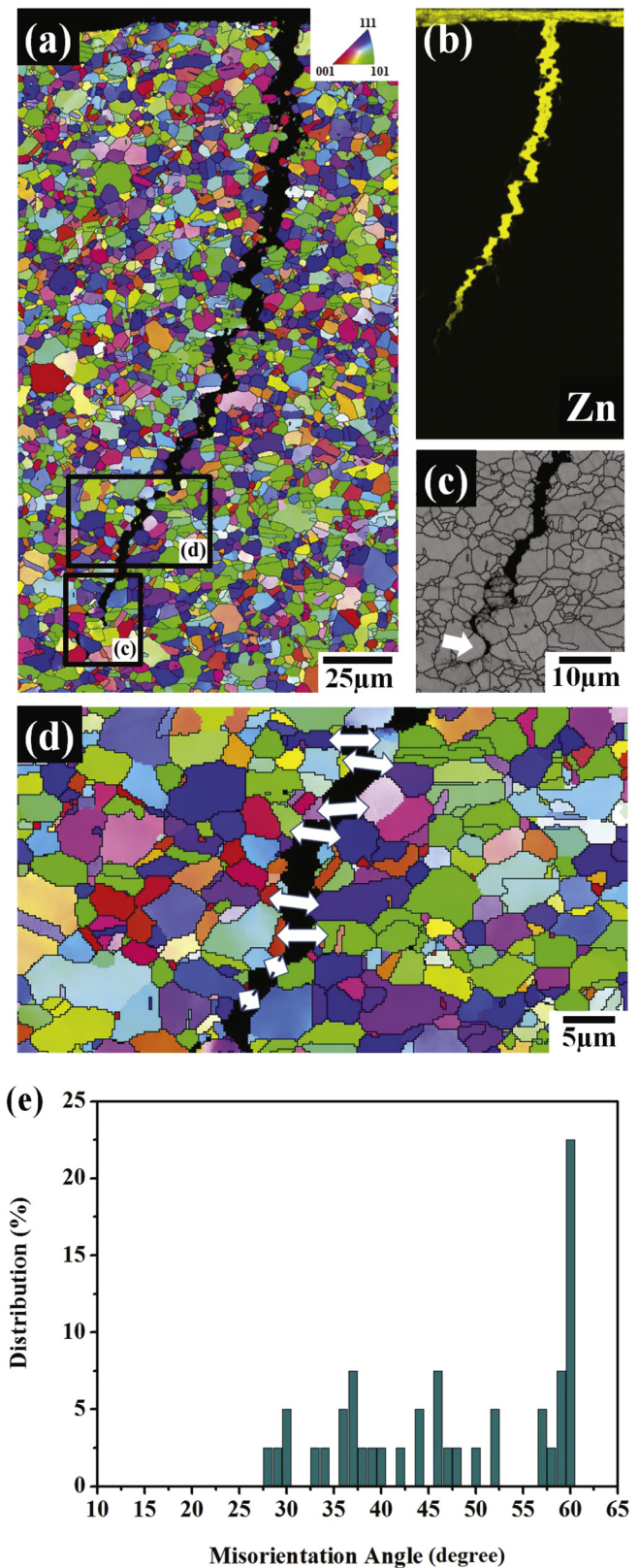
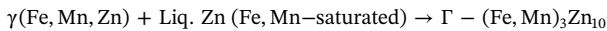


Fig. 7. The overview of EBSD analysis of a representative LME crack, (b) Zn-penetration along the LME crack, (c) IQ map at the tip of the LME crack showing the propagation along the austenite grain boundaries, (d) comparing the matching grains on either side of the LME crack, and (e) distribution of misorientation angles of matched grains along the LME crack.





The proposed mechanism is consistent with the Zn alloy inside the crack has a Zn content of ~70%, and therefore forms  $\Gamma$ -(Fe,Mn)<sub>3</sub>Zn<sub>10</sub>-phase. Even though Zn is a strong ferrite stabilizer, the presence of a significant Mn-content (austenite stabilizer) in the TWIP and MMn-TRIP steels, means that no  $\alpha$ -Fe(Zn) phase forms in the vicinity of the LME crack. The formation of  $\alpha$ -Fe(Zn) within the LME cracking area has been reported in Zn-coated 22MnB5 press-hardening steel [25,26].

The lesser extent to which LME cracking is observed in the TRIP counterpart is attributed to the initial microstructure of its base material. According to Fig. 3a, the initial microstructure of the MMn-TRIP steel is comprised of fine needle-like austenite phase surrounded by a ferrite matrix, and most of the boundaries are inter-phase type. In contrast, the initial structure of the TWIP steel is fully austenitic (Fig. 3b) and therefore, the occurrence of LME is not dependent on the  $A_{c3}$  temperature. In this regard, the plausible explanation for the occurrence of the LME-cracking in the TRIP counterpart relies on the austenite grain boundaries emerged within the HAZ during the heating cycle of LBW. A full austenitic structure would appear within the upper critical HAZ (UCHAZ), where the temperature exceeds the  $A_{c3}$  temperature of the material (~780 °C). The  $\eta$ -phase as the main phase of GI-coating tends to vaporize around 900 °C [27]. Therefore, the temperature window (~750–900 °C) for the concurrency of the presence of liquid Zn and susceptible microstructure (two main prerequisites of LME) is narrow. This, in turn, justifies lower potential of LME-induced cracks in the TRIP-side of the joint.

### 3.4. Grain Boundary Analysis

Fig. 7a and b show the EBSD orientation and corresponding Zn penetration map of a representative LME crack in the TWIP side of the joint. According to the image quality (IQ) micrograph in Fig. 7c, the LME crack propagated intergranularly along austenite HABs (black lines). The overall LME crack propagation path is governed by the direction of the applied tensile stress; however, the local propagation path is governed by the grain boundaries. Hence, to determine the misorientation angle of grain boundaries in which Zn has penetrated, matching grains in both sides of the LME crack has been found. Subsequently, by keeping one of the grains as the reference, the local orientation change between each pair of the matched grains has been compared (Fig. 7d). The distribution of misorientation angles in all the matched grains is shown in Fig. 7e. As is seen, Zn penetration only has occurred in HABs, and none of the LABs contributed in the cracking. Moreover, it has been observed that a considerable fraction of Zn-penetrated grain boundaries showing misorientation angles of about 60°. This is attributed to the presence of incoherent coincidence site lattice (CSL) boundaries in the TWIP steel. It is well-established that due to low stacking fault energy (SFE), TWIP steel shows a high fraction of twinning with a  $\Sigma 3$  (60° [111]) relationship [28,29]. Therefore, it can be concluded that in addition to the general HABs,  $\Sigma 3$  twinning boundaries could play role in Zn penetration along the boundaries. As denoted by Ludwig et al. [30], the thermodynamic driving force ( $F_D$ ) for the liquid metal penetration along the grain boundaries is the energy reduction according to the following equation:

$$\bar{F}_D = \gamma_{GB} - 2\gamma_{S/L} \quad (1)$$

where  $\gamma_{GB}$  is the energy of the grain boundary and  $\gamma_{S/L}$  is the solid/liquid interface energy [30]. Therefore, one may expect that large-misorientation grain boundaries with the higher  $\gamma_{GB}$  end in a higher embrittlement driving force. This explains the occurrence of Zn penetration along general HABs over a certain threshold misorientation angle.

As pointed out, stress-assisted diffusion is responsible for significant Zn diffusion deep into the matrix (up to 450  $\mu\text{m}$ ). It is claimed [21] that the grain boundary diffusion distance in austenite would be around

2  $\mu\text{m/s}$ ; however, the observed penetration depth of Zn in the present study is two orders of magnitude higher than the predicted diffusion distance based on the actual welding time.

## 4. Conclusions

The present study explains mechanism of LME cracking during restrained laser lap joining of high-manganese TWIP and medium-manganese TRIP steel sheets. The major findings are summarized below:

- A direct correlation between the applied external load and LME susceptibility was observed in the TWIP and TRIP steels, however, the TWIP side of the joint showed a higher LME sensitivity compared to the TRIP side.
- Detailed EPMA results indicated the presence of  $\Gamma$ -(Fe,Mn)<sub>3</sub>Zn<sub>10</sub> phase inside the cracks, showing the penetration of liquid zinc during welding. Based on the crack tip analysis, the stress-assisted diffusion of Zn into the austenite grain boundaries and further liquid-Zn formation by a peritectic reaction was determined as the LME-cracking mechanism.
- The distribution of misorientation angles confirmed that Zn penetration only occurs at high angle grain boundaries; however,  $\Sigma 3$  twinning (60°) boundaries also play role in Zn penetration.

## Acknowledgements

Authors would like to acknowledge the International Zinc Association in Durham, NC, USA, and the National Science and Engineering Research Council (NSERC) of Canada for providing the support to carry out this work.

## References

- P. Lan, J. Zhang, Tensile property and microstructure of Fe-22Mn-0.5C TWIP steel, *Mater. Sci. Eng. A* 707 (2017) 373–382.
- H. Liu, J. Liu, B. Wu, Y. Shen, Y. He, H. Ding, X. Su, Effect of Mn and Al contents on hot ductility of high alloy Fe-xMn-C-yAl austenite TWIP steels, *Mater. Sci. Eng. A* 708 (2017) 360–374.
- R. Ueji, N. Tsuchida, D. Terada, N. Tsuji, Y. Tanaka, A. Takemura, K. Kunishige, Tensile properties and twinning behavior of high manganese austenitic steel with fine-grained structure, *Scr. Mater.* 59 (2008) 963–966.
- J.E. Jin, Y.K. Lee, Effects of Al on microstructure and tensile properties of C-bearing high Mn TWIP steel, *Acta Mater.* 60 (2012) 1680–1688.
- M.H. Razmpoosh, A. Zarei-hanzaki, N. Haghdadi, J. Cho, W. Jae, S. Heshmati-manesh, Thermal stability of an ultra fine-grained dual phase TWIP steel, *Mater. Sci. Eng. A* 638 (2015) 5–14.
- M.H. Razmpoosh, M. Shamanian, M. Esmailzadeh, The microstructural evolution and mechanical properties of resistance spot welded Fe-31Mn-3Al-3Si TWIP steel, *Mater. Des.* 67 (2015) 571–576.
- Z.H. Cai, H. Ding, R.D.K. Misra, Z.Y. Ying, Austenite stability and deformation behavior in a cold-rolled transformation-induced plasticity steel with medium manganese content, *Acta Mater.* 84 (2015) 229–236.
- S. Lee, S.J. Lee, B.C. De Cooman, Austenite stability of ultrafine-grained transformation-induced plasticity steel with Mn partitioning, *Scr. Mater.* 66 (2012) 832–833.
- J. Han, Y.K. Lee, The effects of the heating rate on the reverse transformation mechanism and the phase stability of reverted austenite in medium Mn steels, *Acta Mater.* 67 (2014) 354–361.
- C. Beal, X. Kleber, D. Fabregue, M. Bouzekri, Embrittlement of a zinc coated high manganese TWIP steel, *Mater. Sci. Eng. A* 543 (2012) 76–83.
- R. Ashiri, M. Shamanian, H.R. Salimijazi, M.A. Haque, J.H. Bae, C.W. Ji, K.G. Chin, Y. Do Park, Liquid metal embrittlement-free welds of Zn-coated twinning induced plasticity steels, *Scr. Mater.* 114 (2016) 41–47.
- R. Ashiri, M. Shamanian, H.R. Salimijazi, M.A. Haque, C.W. Ji, Y. Do Park, Supercritical area and critical nugget diameter for liquid metal embrittlement of Zn-coated twinning induced plasticity steels, *Scr. Mater.* 112 (2016) 156.
- Y.G. Kim, I.J. Kim, J.S. Kim, Y. Il Chung, D.Y. Choi, Evaluation of surface crack in resistance spot welds of Zn-coated steel, *Mater. Trans.* 55 (2014) 171–175.
- C. Beal, X. Kleber, D. Fabregue, M. Bouzekri, Liquid zinc embrittlement of twinning-induced plasticity steel, *Scr. Mater.* 66 (2012) 1030–1033.
- T. Böllinghaus, H. Herold, C.E. Cross, J.C. Lippold, *Hot Cracking Phenomena in Welds II*, Springer Science & Business Media, 2008.
- N. Lun, D.C. Saha, A. Macwan, H. Pan, L. Wang, F. Goodwin, Y. Zhou, Microstructure and mechanical properties of fibre laser welded medium manganese

- TRIP steel, *Mater. Des.* 131 (2017) 450–459, <https://doi.org/10.1016/j.matdes.2017.06.037>.
- [17] P.J.L. Fernandes, D.R.H. Jones, Specificity in liquid metal induced embrittlement, *Eng. Fail. Anal.* 3 (1996) 299–302.
- [18] S.P. Lynch, Metal-induced embrittlement of materials, *Mater. Charact.* 28 (1992) 279–289.
- [19] Global Welding Standard, Test procedures resistance spot welding of steel, *Glob. Weld. Stand. Test Proced. Resist. Spot Weld. Steel, GWS-5A Stand*, 2011.
- [20] D.C. Saha, E. Biro, A.P. Gerlich, Y. Zhou, Effects of tempering mode on the structural changes of martensite, *Mater. Sci. Eng. A* 673 (2016) 467–475.
- [21] H. Kang, L. Cho, C. Lee, B.C. De Cooman, Zn penetration in liquid metal Embrittled TWIP steel, *Metall. Mater. Trans. A* 47 (2016) 2885–2905.
- [22] S.S.S. Bhan, A. Lal, The Fe-Mn-Zn system, *Phase Diagr. Eval. Sect. II*. 12 1991, pp. 667–672.
- [23] C.W. Lee, W.S. Choi, L. Cho, Y.R. Cho, B.C. De Cooman, Liquid-metal-induced embrittlement related microcrack propagation on Zn-coated press hardening steel, *ISIJ Int.* 55 (2015) 264–271.
- [24] E.E. Glickman, Dissolution condensation mechanism of stress corrosion cracking in liquid metals: driving force and crack kinetics, *Metall. Mater. Trans. A* 42A (2011) 250–266.
- [25] L. Cho, H. Kang, C. Lee, B.C. De Cooman, Microstructure of liquid metal embrittlement cracks on Zn-coated 22MnB5 press-hardened steel, *Scr. Mater.* 90 (2014) 25–28.
- [26] M.H. Razmpoosh, A. Macwan, E. Biro, D.L. Chen, Y. Peng, F. Goodwin, Y. Zhou, Liquid metal embrittlement in laser beam welding of Zn-coated 22MnB5 steel, *Mater. Des.* 155 (2018) 375–383.
- [27] D.W. Fan, B.C. De Cooman, State-of-the-knowledge on coating systems for hot stamped parts, *Steel Res. Int.* 83 (2012) 412–433.
- [28] S. Martin, S. Wolf, U. Martin, L. Kru, Deformation mechanisms in austenitic TRIP/TWIP steel as a function of temperature, *Metall. Mater. Trans. A* 47 (2016) 49–58.
- [29] J. Kim, Y. Estrin, B.C.D.E. Cooman, Application of a dislocation density-based constitutive model to Al-alloyed TWIP steel, *Metall. Mater. Trans. A* 44A (2013) 4168–4182.
- [30] W. Ludwig, D. Bellet, In situ investigation of liquid Ga penetration in Al bicrystal grain boundaries: grain boundary wetting or liquid metal embrittlement? *Acta Mater.* 53 (2005) 151–162.